Weld World (2016) 60:1121–1131
DOI 10.1007/s40194-016-0382-0

RESEARCH PAPER

Production by FSW of free-shape hollow box profile in AA5754 for automotive application

Topi Taavitsainen[1] · **Pedro Vilaça**[1] · **Tommi Mutanen**[2]

Received: 10 January 2016 / Accepted: 24 August 2016 / Published online: 8 September 2016

Abstract In automotive industry, the development of a feasible and reliable solution to produce free-shape hollow box profiles in low thickness AA5754, typical in automotive applications, represents an important innovation opportunity. The main challenge is to produce sound welds between thin plates in a corner joint design, when the activation of the FSW joining mechanisms demands application of a significant mechanical energy. The innovation is based on a new clamping system enabling the use of a conventional tool architecture. The innovation enables to produce hollow box profiles in a wide range of aspect ratios. The cross-section dimensions implemented for the test specimens are 100 mm × 50 mm, with a thickness of 3 mm. The thermal history is monitored at strategic positions along the joint. Metallographic analysis of the weld zone includes EBSD and grain size evaluation. The mechanical properties of the joints are assessed via microhardness and a specially designed bending test: corner opening test (COT). The structural behavior of the final profile is tested with a quasi-static crashworthiness test. The results demonstrate the feasibility of the concept, by presenting a sound weld zone. The FSW components clearly overcome the COT and crashworthiness resistance of similar structures welded by TIG.

Recommended for publication by Select Committee AUTO - Automotive and Road Transport

✉ Pedro Vilaça
pedro.vilaca@aalto.fi

[1] Department of Mechanical Engineering, School of Engineering, Aalto University, Espoo, Finland

[2] Autom Consulting, Vantaa, Finland

Keywords (IIW Thesaurus) Friction stir welding · Clamps · Al Mg alloys · Tubular constructions · Automotive engineering

1 Introduction

Automotive industry's interest in using aluminum alloys in car chassis structures is increasing due to the perceived need to produce more energy efficient vehicles with lower environmental impact [1]. The production of chassis and other automotive structural components based on the typical high strength-to-weight ratio of the aluminum alloys enable to lower the vehicles weight complying with increasing structural safety demands [2]. Another advantage is the high recyclability of the aluminum, associated with the fact that secondary aluminum uses about 7 % of the energy required to produce primary aluminum and reduces emissions [3]. This allows structural design solutions with cost savings and low ecological footprint [4]. The good corrosion resistance of the Al-Mg alloys, such as the AA5754 tested in this work, is also a relevant advantage, mainly when compared with the magnesium alloys that are one other common alternative of lightweight metallic materials for automotive applications [5]. One disadvantage of the structural aluminum alloys is the low weldability by both resistance welding, due to the low electrical resistivity and high thermal conductivity, and fusion welding, due to the softening of the heat-affected zone (HAZ) and high susceptibility for formation of porosity and hot cracking. The friction stir welding (FSW) [6] of aluminum alloys has proven to deliver defect-free joints, with good mechanical properties and low distortion. The thermomechanically affected zone (TMAZ), including the dynamically recrystallized zone (nugget), presents good toughness and formability in both similar [7] and dissimilar welds [8]. Due to the low heat input, the HAZ does not undergo as

severe aging phenomena as in fusion welding processes [9]. The FSW is mostly applied to butt and overlap joints. For overlapped joints, beside the FSW, also the friction stir spot welding (FSSW) is a common solution [10].

One of the challenges of applying the aluminum alloys in automotive industry is that the production of closed hollow profiles, a typical solution to attain the design specifications, is rather difficult except by extrusion for Al-Mg-Si alloys [11]. In this work, the joint design, tool features, and clamping system are developed to allow the production of hollow box profiles in AA5754-H22 with a wall thickness of 3 mm. The new concept enables the application of conventional FSW, discarding complex tool architectures such as bobbin tools [12], stationary shoulder tools [13], or using extrusions [14], in the production of free-shape hollow box profiles, i.e., enabling a wide range of aspect ratios for the box shape. One major potential application of the long hollow box profiles is in chassis for buses and coaches [15].

The technological conditions are discussed along with the analysis of the thermal cycle tests and mechanical power delivered by the tool along the weld cycle [16]. The main metallurgical features of the joints are assessed by optical microscopy and EBSD. The mechanical properties of the joints are presented in terms of microhardness field and corner opening test (COT), a dedicated test solution to evaluate the bending resistance. The resulting welded hollow box structural component is evaluated via quasi-static crashworthiness test, especially relevant for automotive applications.

2 Development of the clamping system

During the FSW process, only mechanical energy is applied into the base materials. Within the processed materials, part of this energy is then transformed into heat and activation of the solid state joining mechanisms. The mechanical energy nature of the FSW demands strong and precise clamping of the components in order to achieve sound welds. One major challenge is to fully close the visco-plastic flow domain within the processed zone, preventing loss of material into flash and maintaining high internal forging pressure, e.g., to avoid internal voids [17]. This challenge is particularly difficult to respect in the FSW of low thickness components in “L” shape joints with conventional architecture tools. Other design specifications for the clamping system are set to fulfill the following objectives:

1. Withstand with no deflection the forces and heat during the weld cycle;
2. Uniform distribution of clamping forces;
3. To enable the clamping of different plate thicknesses in similar and dissimilar joints;
4. To be modular enabling the clamping of workpieces with wide range of dimensions;
5. Repeatability, precision and fast clamping operation;
6. To enable full penetration welds easy to extract from clamping system, e.g., preventing the adhesion of the aluminum to the anvil; and
7. The inner anvil does not need to be removed during the execution of all the welds.

Figure 1 depicts the concept of the clamping system and the real clamping system implemented to perform the welds. The laboratorial clamping system was designed to produce free-shape hollow box profiles with a maximum length of 250 mm. The fixed anvil is attached to the welding machine table. The floating anvil is inside the hollow box profile during all four welds. The main objective of the copper insert(s) is to act as a heat sink. The clamping forces are applied as close as possible to the zone being processed while the rest of the workpieces remain free. In practice, this means that the clamping system enables a wide range of aspect ratios for the box shape. Considering the typical low plate thicknesses in automotive industry, the peripherical zone of the shoulder of the FSW tool will rotate outside the aluminum plates and over the copper insert in the fixed anvil (Fig. 1c). The vertical dimension of this copper insert should be adapted to the thickness of the plates being welded, so that a gap between the shoulder and the copper insert should exist to avoid any direct contact. The key issue is to keep this gap between 0.1 and 0.2 mm, to avoid the flow of aluminum through this gap and thus minimizing the loss of base material into flash.

The clamping system is modular and adding other components is possible, e.g., a second inner anvil may be used. After some iterations in the development of the original design concept, the final clamping system produced fulfilled all the requirements. Further development for the clamping system will include hydraulic actuators to produce uniform clamping forces and reduce the setup time, and a cooling system for optimal thermal management. The clamping system enables welding similar and dissimilar plate thicknesses, which makes production of tailored box-section possible. Other authors [18] show good results with structures like tailor-welded blanks. Tailor-welded blanks are studied mainly as a method to optimize the resistance-to-weight ratio of the structures [19]. This concept of the clamping system enables the use of a conventional tool architecture discarding the need of an expensive bobbin-tool for which life of the probes are compromised by

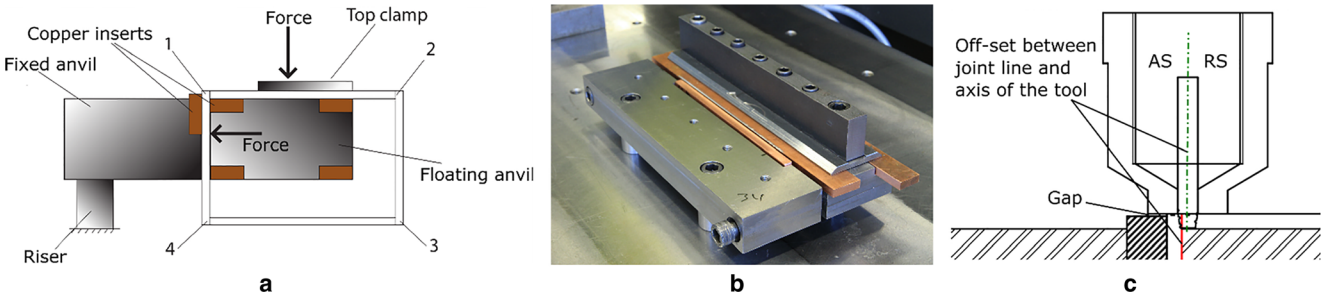

Fig. 1 Dedicated clamping system implemented for production of the free-shape hollow box profiles with maximum length of 250 mm. **a** Schematic representation of the concept. **b** Photo of the final implemented system, as assembled. **c** Details of the joint design associated with the clamping system, with emphasis for the gap between tool shoulder and copper insert in the fixed anvil and of the offset between the joint line and the tool axis

the complex and highly demanding thermal and mechanical loading [20].

3 Methods and experimental conditions

3.1 Base material

The material selected for this study is an AA5754-H22 (EN AW-Al-Mg3) representing one important material for automotive industry. This aluminum grade has typical good mechanical properties and excellent corrosion resistance. The temper for the selected material is H22, that is cold-rolled and annealed to 1/4 hardness. Tensile tests of base material are conducted addressing the yield strength and ultimate tensile strength for the material batch. Yield strength and ultimate tensile strength longitudinal to rolling direction are 170 and 286 MPa, respectively. Yield strength and ultimate tensile strength transversal to rolling direction are 179 and 288 MPa, respectively. Hardness measured for base material is 79 HV05 at top section, 78 HV05 at longitudinal section, and 73 HV05 at transversal section. Plate thickness of 3 mm was selected to be investigated since it is a common thickness in automotive manufacturing, namely in construction of chassis for bus and coaches.

3.2 FSW equipment and parameters

Welding is performed with an Esab Legio 5UT FSW welding machine with maximum forging force of 100 kN enabling alternative control of the vertical forging axis by force, position, and speed. The welds are made according to ISO 25239:2011. The FSW tool used is based on modular design enabling the combination of different shoulders and probes features and fine tuning of probe length with 0.1-mm increments [21]. This modular tool design is dedicated for R&D on FSW of aluminum alloys. Considering that the tool geometry and features have major role in the quality of the FSW joints in aluminum alloys, this tool enables the optimization of the processing conditions and penetration. The tool material is AISI H13 quenched and tempered to hardness over 50 HRC. The final tool dimensions and features are selected as the best ones from a comprehensive and systematic experimental analysis. As depicted in Fig. 2, the tool features are as follows: (i) the probe is conical with diameter from 4 down to 3 mm along a length of 2.9 mm with 1.5 pitch scrolls and (ii) the shoulder diameter is 15 mm. The shoulder is planar with 2 CCW scrolls with pitch 2 (half rotation between inner and outer shoulder diameter). The scrolls shape are triangular isosceles with high of 0.9 mm. This design of the shoulder discards the need of a tilt angle to perform the welds and thus enables welding in any direction with CW rotation.

The AA5754-H22 plates are milled to the dimensions of 200 mm × 100 mm and 200 mm × 50 mm, ensuring good fitting between abutting surfaces. Workpieces are cleaned with ethanol before welding. The welding parameters are as follows: (i) spindle rotation speed, $\Omega_{spindle}$ = 1200 rpm (CW); (ii) welding speed, v_{weld} = 250 mm/min; (iii) FSW control: axial force, F_z = 5 kN; (iv) plunge control: position, plunge depth 2.9 mm; (v) plunge speed 0.1 mm/s; and (vi) dwell time, T_{dwell} = 5 s.

As represented in Fig. 1c, the position of the tool axis in relation to the joint line and location of the retreating/advancing side of the tool are key issues supporting the success of the clamping system solution. To enable full containing of the visco-plastic flow of material and avoid generation of excessive flash, the following conditions should be attained: (i) the advancing (shear) side of the welds have to be positioned in the outer anvil side and (ii) a small tool axis offset to weld joint line should exist bias to inner anvil, i.e., retreating (flow) side of the welds. The best offset value found is 1.1 mm.

4 Testing plan

The length of the hollow box profiles produced for testing is 200 mm, with cross section of 100 mm × 50 mm made of 3-mm-thick plates. All the four welds have a length of about

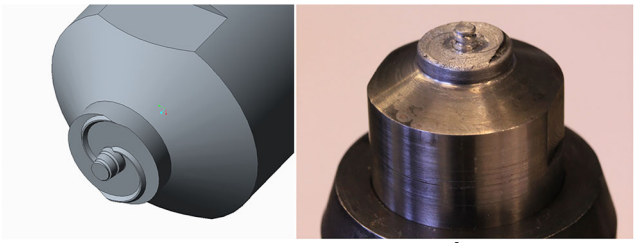

Fig. 2 FSW tool implemented to produce the free-shape hollow box profiles. **a** Schematic representation of the shoulder and probe features. **b** Photo of the tool as extracted from the weld

170 mm. During the welds, the mechanical loads and temperature history are monitored. The thermal cycle is measured with Graphtech GL800 data acquisition system with 12 K-type thermocouples, located at the top surface and root of the joint, according to the plan presented in Fig. 3. The thermocouples located at the root were inserted through the copper heat sinks and locked at the root surface during the clamping of the plates.

For the tests based on cross-sectional analysis, i.e., optical microscopy, EBSD and hardness, the cross section is extracted from about the middle of the weld joint. The samples are prepared for optical microscopy by cutting perpendicular to processing direction and grinding with Tegramin automated station. Polishing is done by hand with 1200–2000–4000 grit papers and fine polishing with 3 and 1 μm diamond paste. The optical macrographs are taken from specimens using Nikon Epiphot 200 inverted metallurgical microscope. The microscope is equipped with Nikon DS-U1 digital sight. The EBSD studies are performed with Zeiss Ultra FEG-SEM equipped with Nordlys detector and Channel 5 software, and the sample preparation procedure for EBSD is similar to macroscopic samples. The polishing is finished with 1/4 μm diamond paste and 40 h in silica compound to remove all residual deformation from the sample surface and the sample surface is not etched. Preparing the sample is done with care to prevent any deformation on the sample surfaces The microhardness testing is performed with CSM instrumented platform with micro-combi testing head equipped with Vickers indentator. Equipment uses indentation depth and Oliver & Pharr method to calculate hardness value. The platform includes an optical video microscope, X, Y, and Z automated tables and antivibration table. Testing load is set to 50 g and pause 10 s.

From the conventional mechanical testing methods, only the measurement of the hardness field in the vicinity of the weld zone is applied, because others, such as uniaxial tensile and bending testing, do not apply directly to the "L" joint configuration. To complement the characterization of the mechanical performance under quasi-static loading, two other tests are implemented, namely the corner opening test (COT) and the quasi-static crashworthiness tests. The COT promotes the bending of the weld joint with the root of the welds under tensile which corresponds to the most demanding loading situation. The results are mostly sensitive to root defects such as lack of penetration (LOP) and internal voids. The COT is done with MTS 810 servo-hydraulic universal testing machine equipped with purpose-built testing rig including linear rolling guides and cars (Fig. 4). During the COT, the built-in data acquisition system is used to record force and displacement data. The force-displacement data is treated with MATLAB software for plotting force-displacement curves and calculate absorbed energy during test. Because there are no standards for the COT, it was decided to extract specimens with dimension of 40 mm in each leg and 40 mm in width (see Fig. 4a). Considering the 170 mm length welds, three

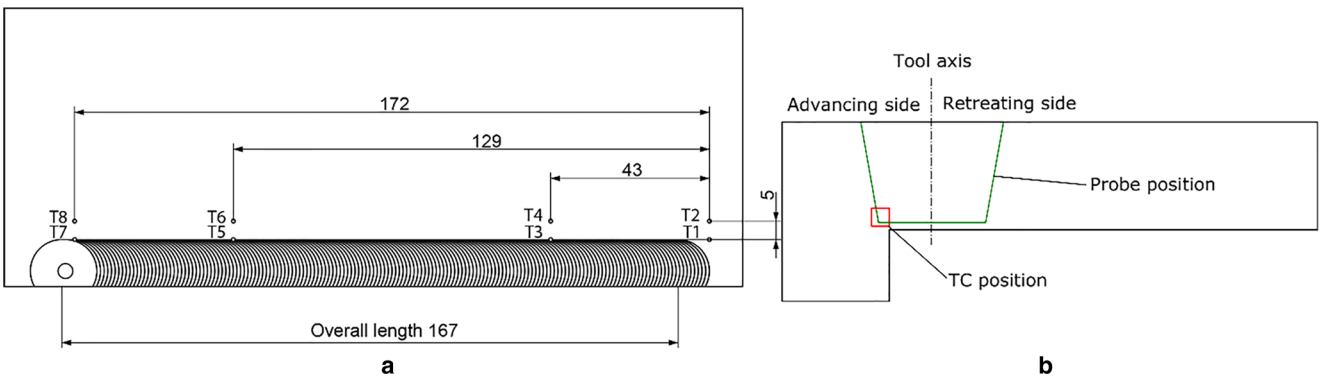

Fig. 3 Positioning plan of the 12 K-type thermocouples (TC's), located in the vicinity of the joint. **a** 8 TC's (T1 ... T8) located at the top surface. **b** 4 TC's (R1 ... R4) located at the root in the same cross sections as for the top surface

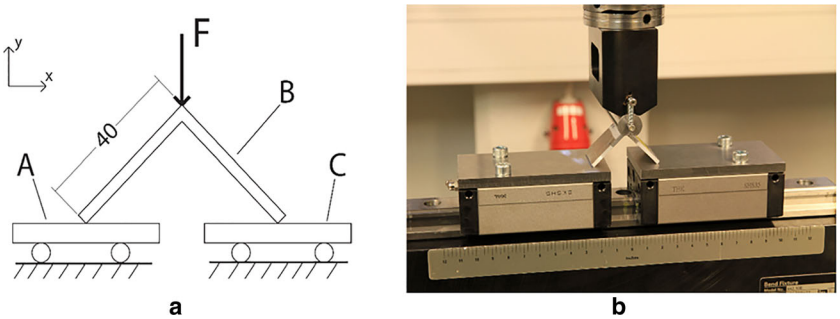

Fig. 4 Corner opening test (COT) apparatus. **a** Schematic representation of the test conditions. **b** Photo of COT setup

specimens for the COT are extracted, namely (1) about 45 mm from the starting point of the weld, (2) from the middle, and (3) about 45 mm from the end.

The quasi-static crashworthiness tests, as depicted in Fig. 5, are performed to assess the buckling behavior (modes and stability), structural integrity, and energy absorption capacity. These tests are typical in the analysis of the structural performance of key automotive components. The crashworthiness tests are applied to the box profiles with length of 160 mm, after extracting 20 mm from both ends. Quasi-static crashworthiness test are performed with servo-hydraulic testing rig with external extensometers and force data acquisition system. Cross-head downwards speed is set to 5 mm/min [22]. Boundary conditions are presented in more detail in Fig. 4b. Some 5-mm deep grooves are manufactured to upper and lower anvil (Fig. 4a, A and C) to prevent sliding. Lower anvil is fixed to the ground and upper anvil is free to translate and rotate in all directions. Test sample has 150 mm of free length in the start of testing. In Fig. 4b and c, the actual testing equipment is shown.

For COT and crashworthiness tests comparison of FSW with other alternative conventional fusion welding technique, the same corner joints are welded by a qualified welder with manual TIG according to ISO 9692-3:2013 to produce the same size of the box shape hollow profiles. The parameters for the TIG weld joints are as follows: (i) I = 90 A; (ii) V = 13.8 V; (iii) weld speed, v_{weld} = 150 mm/min; (iv) shielding gas: 100 % Ar; and (v) filler wire: OK Tigrod 5356 (ISO 18273:2004), $Ø$ = 2.4 mm. The TIG welding parameters and procedure resulted in full penetration welds. Additionally, for the COT, the FSW joints are compared with similar structural design produced by direct bending of the base material with a bending radius of 5 mm.

5 Results

5.1 Heat input and thermal cycle

Based on Fig. 6, the heat input (HI) value calculated during the FSW is around 840 J/mm, corresponding to a mechanical power (P_{mech}), delivered by the tool into the workpieces of about 3.5 kW, during the weld period. The mechanical power (P_{mech}) is calculated via: P_{mech} [W] = T [$N.m$] × $\Omega_{spindle}$ [rpm] × 2π / 60. The heat input (HI) is determined via: HI [J/mm] = P_{mech} [W] × 60 / v_{weld} [mm/min]. The spindle torque, T [$N.m$], spindle rotation speed, $\Omega_{spindle}$ [rpm], and welding speed, v_{weld} [mm/min], are continuously monitored by the FSW machine, with a rate of 10 Hz.

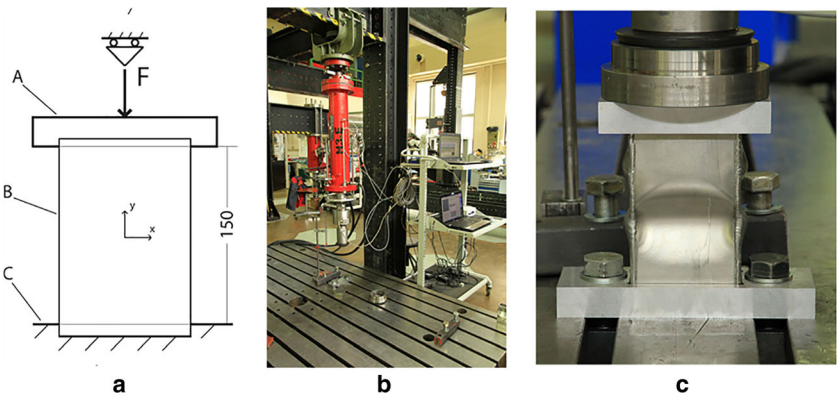

Fig. 5 Quasi-static crashworthiness testing apparatus and boundary conditions. **a** Schematic representation of the boundary conditions during the test. **b** Photo of the global setup. **c** Detail of the test conditions around the test specimen welded with TIG

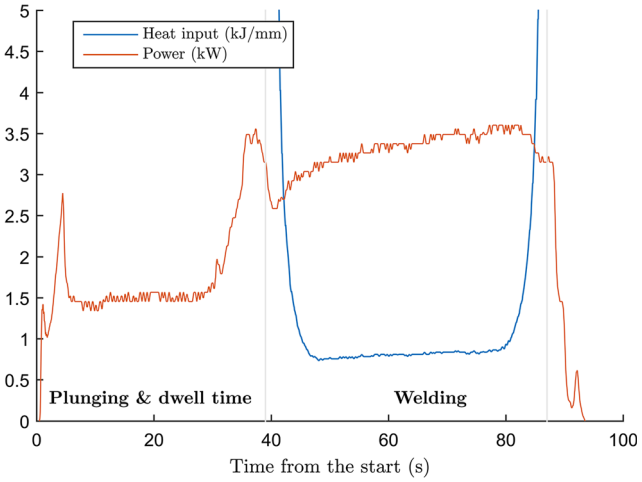

Fig. 6 Monitoring of mechanical power delivered by the tool into the workpieces during FSW

The results from thermal cycle test presented in Fig. 7, for both top surface and root zone, contain significant information concerning the analysis of the stability of the process along the weld seam. The transient effect at both start and end zone of the weld joints is clear and relevant. At the start, and due to the plunge of the tool and mainly the dwell period, when the shoulder is already in full contact with the workpieces, the temperature rises locally. The local influence of the shoulder is emphasized by comparing the pre-heat effect at the top surface (T1 and T2) and at the root (R1). The temperature history obtained for the middle thermocouples located 43 mm from the end do not exhibit any effect from both pre-heat and ending boundary condition. Thus, the values from T5, T6, and R3 stand for the stationary condition. The maximum peak temperature obtained is 280 °C. This value is obtained at the edge of the retreating side of the shoulder for thermocouple T3. For the stationary condition, at the same position, the peak temperature obtained is 240 °C. The peak temperature obtained at the edge of the retreating side of the shoulder is typically 100 °C higher than the ones at the top surface but 5 mm far from this point, and 50 °C higher than at the root. In general, the heating and cooling rates near the peak temperatures are not depending on the thermocouple position. The start and end transient conditions only shown to affect the heating and cooling rates at lower temperature levels.

5.2 Metallographic analysis

Figure 8 presents one representative macrograph from the optical microscopic analysis. This figure represents the typical macrographs of all the sound welds (e.g., no internal voids) inspected at the middle and at the end of the weld. Figure 8 depicts a fully developed nugget region over all the thickness (full penetration), with evidence of the lateral offset in relation to the original joint line. An alignment of particles exists at the root of the weld, but with an offset from the original joint line. This fact is relevant because the original joint line is fully processed. There is an evident tail of the nugget near of the top face of the advancing side of the joint.

The EBSD (electron backscatter diffraction) studies depicted in Fig. 9 are performed to analyze the microstructure over the cross section of the FSW joint. The sampling area for the EBSD analysis is shown in Fig. 9a. From the analysis of the EBSD images, it is not evident any texture effect both at the HAZ and TMAZ, including the dynamically recrystallized zone (DRX) [23] of the TMAZ, i.e., the weld nugget. The grain size over the scanning area is presented in Fig. 10. This figure emphasizes the small equiaxed grain size in the nugget (≤2.1 μm) when compared with the original base material (12.5 μm). The grain size refinement is a known phenomenon in FSW [24–26]. In this figure, the width and the position of the probe is included. On the advancing side of the

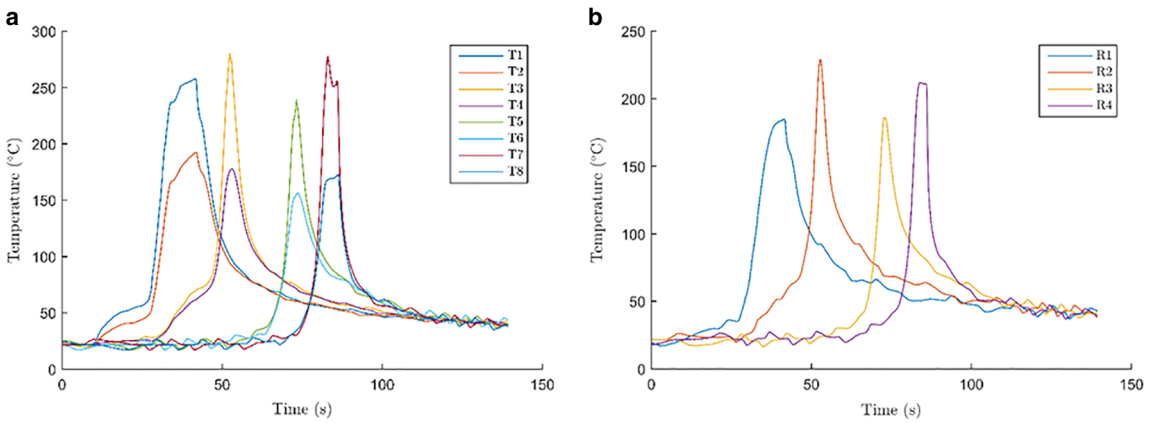

Fig. 7 Thermal history during FSW. **a** 8 TC's (T1 ... T8) located at the top surface. **b** 4 TC's (R1 ... R4) located at the root in the same cross sections as at the top surface

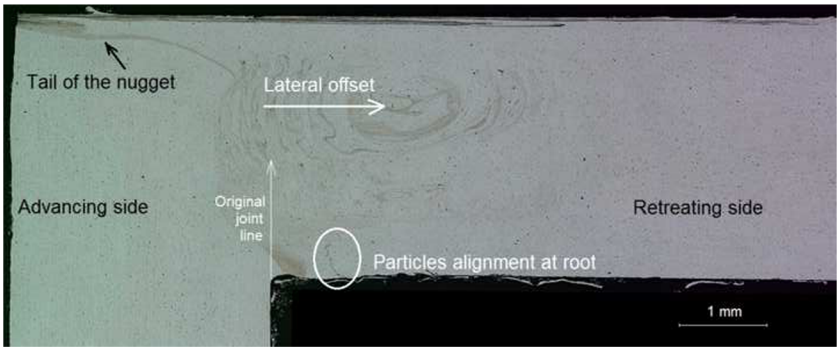

Fig. 8 Optical macrograph of the cross section from the middle of the weld

probe, the gradient in the grain size is high and the width of the zone with refined grain size is narrower than on the retreating side of the probe. The processed material volume on the retreating side is significantly higher than on the advancing side. This is due to asymmetric nature of the FSW process, majority of the material flow on the retreating side, thus the evidence of material flow is more pronounced. This can be observed also in Fig. 9b and d. The difference in the grain size of the base material and of the processed zone is substantial. The minimum grain size can be smaller than the measured since the resolution (step size) of the measurement is coarser than recommended. The minimum is ten pixels per grain [27]. The effect of the grain refinement is evident nevertheless.

5.3 Microhardness

Figure 11 presents the distribution of the microhardness in the vicinity of the weld joint. The results show significant increase in hardness of the material directly processed by the probe of the tool when compared with the original base material hardness which is about 73 HV (in the transversal section). In the nugget zone, the average hardness is about 110 HV with a maximum hardness of about 130 HV. The remaining zone of the TMAZ in contact with the shoulder exhibits values of about 100 HV. Other authors also published similar results in FSW of Al-Mg aluminum alloys, mainly associated with the grain refinement and dynamic recrystallization (DRX),

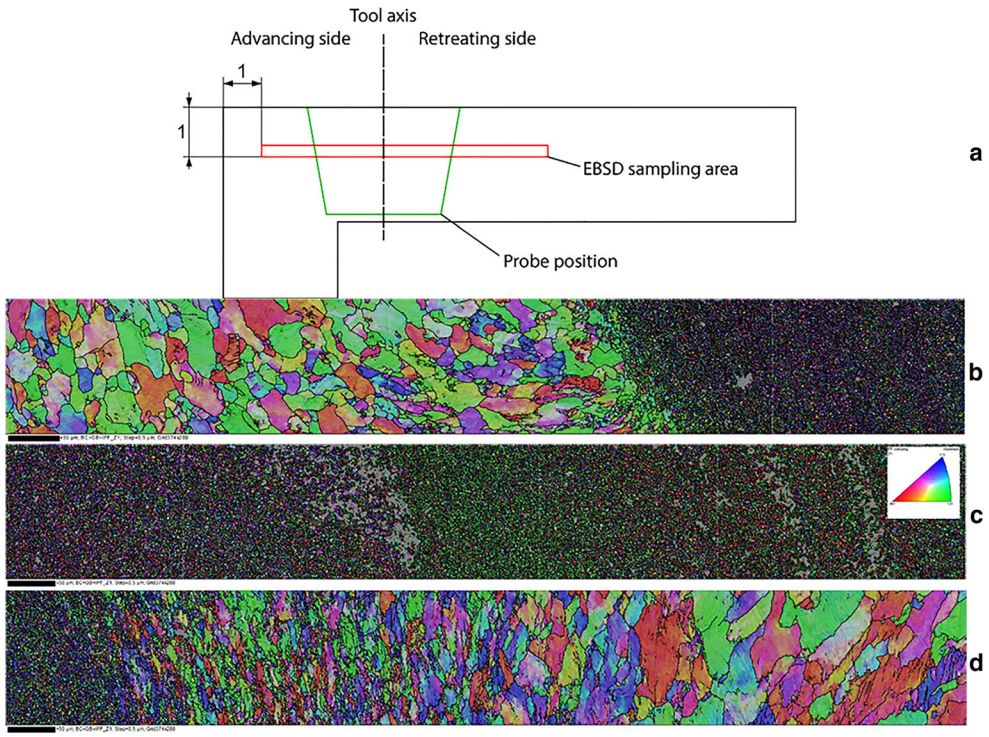

Fig. 9 Metallurgical EBSD analysis. **a** Sampling plan. **b** HAZ and TMAZ at advancing side. **c** Weld nugget with IPF key. **d** HAZ and TMAZ at advancing side

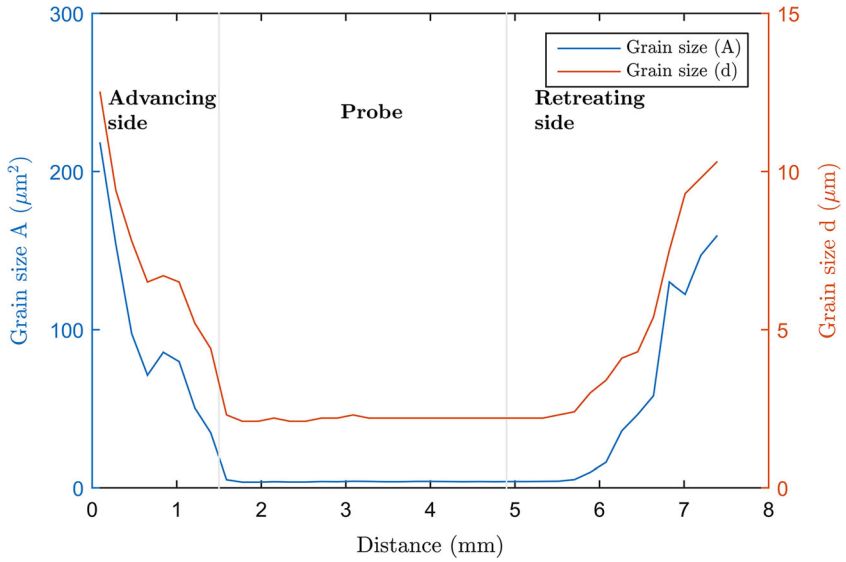

Fig. 10 Grain size over the TMAZ, focusing the weld nugget zone

typically found in the TMAZ of FS welds. There is a distinct hardness gradient at the top surface of the retreating side, localized in the material near the periphery of the shoulder. This hardness gradient may be due to local high strain rates and formation of some flash, which is prone to concentrate in this location, along the weld seam.

Furukawa, Horita, Nemoto, Valiev, and Langdon [28] measured the Vickers microhardness in Al-3 % Mg solid solution alloy subjected to intense plastic deformation and demonstrate conclusively that the Hall-Petch relationship is an appropriate description of the hardness of the material down to the finest grain size examined experimentally (90 nm). Based on the Hall-Petch relationship proposed by [28]: $HV = 43.6 + 48.2/\sqrt{d}$, where [$d$] = μm, the average hardness measured in the nugget region (110 HV) should corresponds to a grain size of about 0.5 μm. This estimative is in agreement with the measurements in the EBSD tests.

5.4 Corner opening tests (COT)

Standard mechanical testing methods for this joint type do not exist, thus COT is used to compare FSW samples to TIG welded and mechanically bended structures with a similar geometry. Figure 12 presents the force versus displacement for the three different welds by FSW, three different welds by TIG, and three different mechanically bended specimens. One other important information from these graphs is the total energy absorbed by the specimen before failure. For each of the three FS welds, COT results are also evaluated at three different regions of the weld joint, namely, start, middle, and end region. From these results, it is possible to conclude that the FS welded samples, with about 27 J, are almost as good as bended samples (about 30 J), even with sharp corner geometry that is substantially more susceptible for stress concentration. Bended samples have some radius in the corner and FS welded samples have sharp corners. The samples with the lowest amount of energy absorbed in this test are the TIG welded samples with about 10 J. The TIG welds have a smaller maximum force (about 0.8 kN) and do not present the quasi-perfect plastic regime of the FSW, i.e., after achieving maximum value, the force undergoes a negative gradient until failure. If the mechanical bending of the base material represents the optimal behavior, then this behavior is very similar to the one obtained for the good FS welds, but with a maximum load of about 1.5 kN.

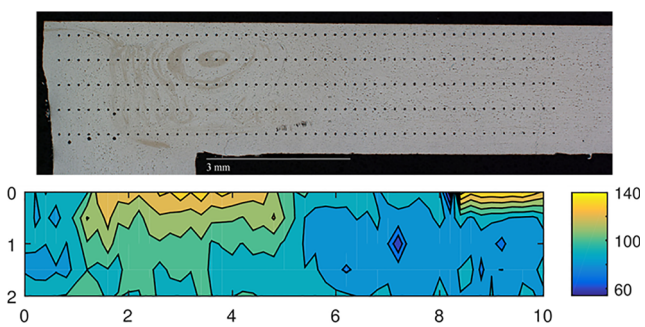

Fig. 11 Vickers microhardness HV05 map

5.5 Quasi-static crashworthiness test

The quasi-static crashworthiness tests are performed for FS welded and TIG welded box shape hollow profiles samples. Samples after testing are shown in Fig. 13. Different buckling modes produced in FS welded samples are shown in Fig. 13a, and failure in the base material of

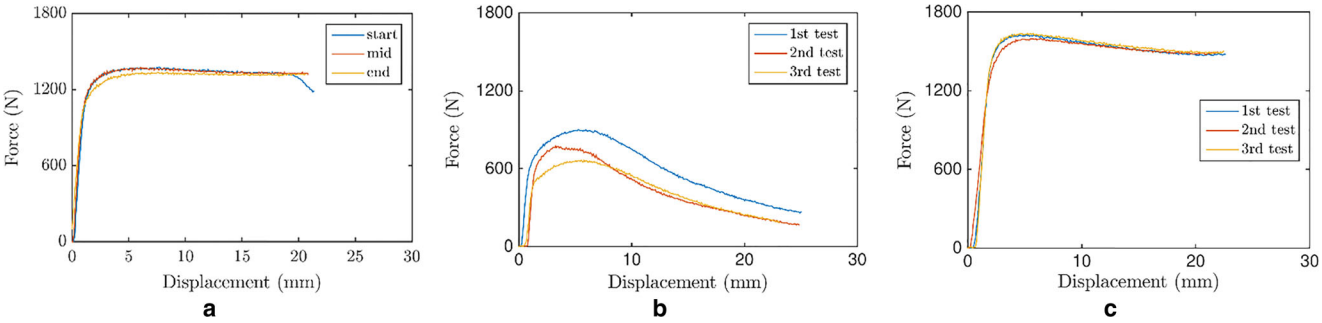

Fig. 12 Force-displacement plots from corner opening tests (COT). **a** COT of FSW welded samples. **b** COT of TIG welded samples. **c** COT of bended base material specimens

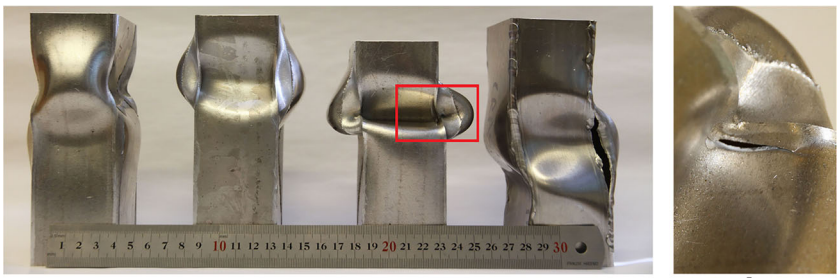

Fig. 13 Test specimens condition after quasi-static crashworthiness tests. **a** Order from left to right: FSW1crash, FSW2crash, FSW3crash and TIG2. **b** Detail of failure marked in (*a*) with *red rectangle*

sample FSW3crash is shown in Fig. 13b. FS welded samples withstand more displacement without failures. TIG welded samples lost their stability around 13 mm of displacement and test is aborted. The Fig. 14 exhibits the force-displacement plots derived from crashworthiness tests. FS welded starts buckling at significantly higher loading than TIG welded counterparts. This behavior is due the fact that FS welded samples have a better dimensional accuracy and less imperfections. Force needed to start buckling in FS welded samples is near 150 kN and tensile yielding strength of the material times the area of cross-section results force of 155 kN. Calculated from the data presented in Fig. 14 the energies absorbed by structures up to 10 mm of displacement are about 940 ± 46 J for the FSW welded components and 800 ± 33 J for the TIG welded components. This difference in the energies absorbed between FS welded samples and TIG welded ones is due to imperfections introduced to the structure by TIG welding.

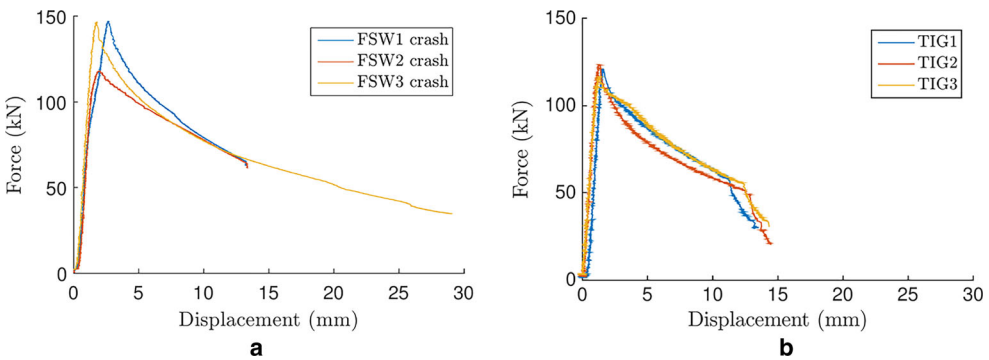

Fig. 14 Force-displacement plots from quasi-static crashworthiness tests. **a** FSW welded samples. **b** TIG welded samples

6 Conclusions

The most significant observations from the present study are the following:

- The new clamping system enables the production with conventional FSW tools of sound hollow box profiles in AA5754-H22 with 3 mm in thickness. This fact represents a good opportunity for innovation in automotive structural design;
- The best technological conditions and parameters resulted in FSW joints with full penetration and no alignment of particles at the root along the original joint line;
- The estimated heat input during the FSW was about 840 J/mm and the results from thermal analysis showed clear transient zones at both start and end zone of the weld joints;
- The EBSD analysis emphasized the small equiaxed grain size in the nugget (≤2.1 μm) when compared with the original base material (12.5 μm). No evident texture is present. On the advancing side, the grain size gradient is higher, and the width of the zone with refined grain size is narrower, than on the retreating side of the probe;
- The hardness in the TMAZ increased from the 73 HV of base material into an average value of 110 HV with a maximum of 130 HV;
- A non-standard corner opening tests is developed and implemented. The results show that the FS welds present an elastic-perfect plastic behavior similar as bended base material (even considering the sharp corner geometry) and significantly overcoming alternative application of TIG welding;
- The critical buckling load of the FSW box profiles during the quasi-static crash worthiness tests is close to the yield limit and the factures are localized away from the TMAZ of the FSW joints. The buckling of all the FSW box profiles during the quasi-static crashworthiness tests retain the axial symmetry. These facts comply with the high demanding requirements of automotive structural design.

Acknowledgments The authors want to acknowledge the funding and technical support by Kabus Oy, Finland, on the scope of the Kabustir project.

References

1. Miller W, Zhuang L, Bottema J, Wittebrood A, De Smet P, Haszler A, Vieregge A (2000) Recent development in aluminium alloys for the automotive industry. Mater Sci Eng A 280(1):37–49
2. Carle D, Blount G (1999) The suitability of aluminium as an alternative material for car bodies. Mater Des 20(5):267–272
3. M. E. Schlesinger (2013) Aluminum recycling. CRC Press
4. Jirang C, Roven HJ (2010) Recycling of automotive aluminum. Trans Nonferrous Metals Soc China 20(11):2057–2063
5. F. Nascimento, P. Vilaça, F. Pires, J. S. Fernando, and L. Quintino (2014) Development of FSW parameters for AZ31 mechanical and corrosion properties. IIW 2014, Doc III-B-03-14. Seoul, South Korea
6. P. Vilaça, W. Thomas (2012) State-of-the-art in FSW technology In: Moreira PMGP et al (ed) Structural Connections for lightweight metallic structures. Springer, pp 85–124
7. Barlas Z, Ozsarac U (2012) Effects of FSW parameters on joint properties of AlMg3 alloy. Weld J 91(1):16s–22s
8. Pandya SN, Menghani JV (2013) Friction stir welding of dissimilar 5xxx to 6xxx al alloys: a review. Applied Mechanics and Materials 376:42–48
9. Barnes T, Pashby I (2000) Joining techniques for aluminium spaceframes used in automobiles: part I—solid and liquid phase welding. J Mater Process Technol 99(1):62–71
10. Klobčar D, Tušek J, Smolej A, Simončič S (2014) Parametric study of FSSW of aluminium alloy 5754 using a pinless tool. Welding in the World 59(2):269–281
11. Ke D, Hengcheng L, Qiumin J, Yun T (2010) Effect of hot extrusion on mechanical properties and microstructure of near eutectic Al–12.0 % Si–0.2 % Mg alloy. Mater Sci Eng A 527(26):6887–6892
12. A. Toskey, W. Arbegast, C. Allen, and A. Patnaik (2005) Fabrication of aluminum box beams using self-reacting and standard fixed pin friction stir welding. In Friction stir welding and processing III as held at the 2005 TMS annual meeting. pp 171–178
13. Wu H, Chen Y-C, Strong D, Prangnell P (2015) Stationary shoulder FSW for joining high strength aluminum alloys. J Mater Process Technol 221:187–196
14. M. Kumagai and S. Tanaka (1999) Properties of aluminum wide panels by friction stir welding. In Proceedings of the first international symposium on friction stir welding, paper. pp S3–P2
15. I. McGregor, D. Nardini, Y. Gao, and D. Meadows (1992) The development of a joint design approach for aluminium automotive structures. Technical report (No. 922112). SAE Technical Paper
16. Vilaça P, Quintino L, dos Santos JF, Zettler R, Sheikhi S (2007) Quality assessment of friction stir welding joints via analytical thermal model, iSTIR. Mater Sci Eng A 445-446:501–508
17. Kim Y, Fujii H, Tsumura T, Komazaki T, Nakata K (2006) Three defect types in friction stir welding of aluminum die casting alloy. Mater Sci Eng A 415(1):250–254
18. Chan S, Chan L, Lee T (2003) Tailor-welded blanks of different thickness ratios effects on forming limit diagrams. Materials processing technology 132(1):95–101
19. Saunders FI, Wagoner R (1996) Forming of tailor-welded blanks. Metall Mater Trans A 27(9):2605–2616
20. T. Neumann (2009) Friction stir welding of Al 2024-T351 using a self-reacting bobbin tool. PhD thesis, Technical University of Ilmenau
21. P. Vilaça, T. Santos (2008) Patent PT 104072: Adjustable modular non-consumable tool with enabling refrigeration for friction stir welding and processing
22. Guillow S, Lu G, Grzebieta R (2001) Quasi-static axial compression of thin-walled circular aluminium tubes. Int J Mech Sci 43(9):2103–2123
23. R. S. Mishra and M. W. Mahoney (2007) Friction stir welding and processing. ASM International
24. Mishra RS, Ma Z (2005) Friction stir welding and processing. Materials science and engineering: R: reports 50(1):1–78

25. Hirata T, Oguri T, Hagino H, Tanaka T, Chung SW, Takigawa Y, Higashi K (2007) Influence of friction stir welding parameters on grain size and formability in 5083 aluminum alloy. Mater Sci Eng A 456(1):344–349
26. Jata K, Semiatin S (2000) Continuous dynamic recrystallization during friction stir welding of high strength aluminum alloys. Scr Mater 43(8):743–749
27. Humphreys F (2001) Review grain and subgrain characterisation by electron backscatter diffraction. J Mater Sci 36(16):3833–3854
28. Furukawa M, Horita Z, Nemoto M, Valiev R, Langdon T (1996) Microhardness measurements and the Hall-Petch relationship in an Al–Mg alloy with submicrometer grain size. Acta Mater 44(11): 4619–4629